Integrating Materials and Manufacturing Innovation (2019) 8:1–16
https://doi.org/10.1007/s40192-019-0124-4

TECHNICAL ARTICLE

Integrative Materials Design of Three-Phase Mo-Si-B Alloys

K. A. Brindley[1] · **M. W. Priddy**[2] · **R. W. Neu**[1,3]

Received: 8 November 2018 / Accepted: 2 January 2019 / Published online: 12 February 2019

Abstract

Mo-Si-B alloys can offer higher temperature capability than Ni-base superalloys with proper balancing of the creep, ductility, and oxidation resistance through microstructure optimization. Mo-Si-B alloys are heterogeneous, containing both brittle and ductile phases and interfaces. Therefore, the phase fractions, their distributions, and their constitutive properties over the range of room temperature to maximum use temperature must be considered. This work addresses the optimization of mechanical properties for three-phase Mo-Si-B alloys. Three modeling tools are employed: microstructure generators to re-create statistically realistic microstructures, crystal viscoplasticity constitutive equations implemented for use with finite element solvers to capture microplasticity, and reduced-order models for evaluating important mechanical properties. In particular, the effects of microstructure on elastic modulus, yield strength, fatigue resistance, and susceptibility to brittle microcracking are considered. A novel reduced-order model is introduced for the evaluation of susceptibility to microcracking at phase interfaces. It is found that the Si content of the α-Mo phase is much more significant to the alloy's balance of mechanical properties than the α-Mo volume fraction.

Keywords Mo-Si-B alloys · Molybdenum-silicide alloys · ICME · Structure-property relationships

Introduction

Refractory metals and their alloys offer higher temperature alternatives to Ni-base superalloys [1–6]. In particular, Mo-Si and Mo-Si-B intermetallics offer oxidation and creep resistance at temperatures up to 1300 °C [3, 7, 8], which is approximately the melting temperature of Ni-base superalloys [1, 6]. However, these intermetallics present a significant design challenge due to their low ductility and low fracture toughness at room temperature [3]. A balance of high-temperature and low-temperature mechanical properties may be achieved in Mo-Si-B alloys by including the more ductile α-Mo phase in addition to the intermetallic phases [3, 7, 8]. However, balancing the oxidation resistance, creep resistance, and damage tolerance requires careful microstructure optimization.

Of the numerous studies on the development of three-phase Mo-Si-B alloys [7, 9–20], perhaps the most promising of Mo alloys is a three-phase microstructure consisting of the intermetallic Mo_3Si and Mo_5SiB_2 (T_2) phases in a continuous α-Mo matrix [12, 18, 19, 21, 22]. Consequently, the material chosen for the focus of this research is a equiaxed, randomly textured, three-phase Mo-Si-B alloy with a continuous α-Mo matrix with average grain diameters of 10 µm and containing the intermetallic Mo_3Si and T_2 phases with average grain diameters of 8 µm. These alloys are typically created using powder metallurgy because it has proven difficult to create the desired α-Mo matrix using melt-based processing and hot working [7, 23, 24].

The α-Mo phase is a solid solution of Si in Mo. This body-centered cubic (BCC) phase is key to providing the ductility and fracture toughness for three-phase Mo-Si-B alloys; however, it oxidizes readily above 600 °C and has poor creep resistance at high temperatures [3, 25]. The strength of the α-Mo phase is highly dependent on Si content, where as little as 1 wt.% Si can increase the yield strength to nearly 1000 MPa from the 400 MPa of pure

✉ K. A. Brindley
kbrindley@gatech.edu

[1] The George W. Woodruff School of Mechanical Engineering, Georgia Institute of Technology, 801 Ferst Drive, Atlanta, GA 30332, USA

[2] Department of Mechanical Engineering, Mississippi State University, 479-1 Hardy Road, Mississippi State, MS 39762, USA

[3] School of Materials Science and Engineering, Georgia Institute of Technology, 771 Ferst Drive, Atlanta, GA 30332, USA

Mo at room temperature [25]. However, adding Si also decreases the fracture toughness and ductility. It has been shown that the addition of 0.5 wt% Si will reduce the room temperature ductility of α-Mo from 25 to 3% [26, 27]. The reduced fracture toughness and ductility is partially attributed to Si segregation to grain boundaries [15, 25, 28]. Non-uniform distribution of dissolved Si within grains and throughout the matrix phase may also appear due to sluggish kinetics [15].

The intermetallic Mo_3Si phase is an A15 cubic phase. Although only a few mechanical properties have been quantified for this phase at high temperature, the room temperature properties of single crystal Mo_3Si specimens have been investigated [29]. This phase is brittle and strong at room temperature and high temperatures. At 1325 °C, Mo_3Si has a yield strength of over 700 MPa and shows little plasticity under deformation due to a small number of active slip systems [3, 30]. The Si in this phase provides oxidation resistance by forming a nanoporous SiO_2 scale over the oxidizing surface [3, 8, 31].

The intermetallic Mo_5SiB_2 (T_2) phase has a body-centered tetragonal structure. Similar to the Mo_3Si phase, this phase is strong and brittle from room temperature up to temperatures of 1500 °C [32]. High-temperature mechanical properties have been explored to determine the elastic constants from room temperature up to 1100 °C [32]. The importance of the T_2 phase is to provide high-temperature strength and oxidation resistance [3]. The T_2 phase provides oxidation resistance by forming a borosilicate scale in the early stages of oxidation. This scale then diffuses into the SiO_2 scale formed by Mo_3Si, which lowers the viscosity of the SiO_2 scale and leads to passivation of the scale [3, 8, 31].

The intermetallic silicide phases are necessary to improve the high-temperature oxidation resistance and creep resistance; however, these intermetallics are brittle even at high temperatures [17, 32]. Consequently, creating a Mo-Si-B alloy for use in the hot section of gas turbine engines requires an optimization of the microstructure between the competing properties of damage tolerance, strength, fatigue resistance, oxidation resistance, and creep resistance. In the development of Mo-Si-B alloys, single property optimizations targeting oxidation resistance have been explored experimentally and through kinetics models [23, 24, 31, 33, 34], in some cases demonstrating reasonable oxidation resistance with as much as 50% α-Mo volume fraction [33]. While some experimental investigations on fracture toughness and damage tolerance have been conducted [12, 18, 22, 35], there has not been much work done to develop microstructure-sensitive modeling tools for the toughness and damage tolerance of Mo-Si-B alloys suitable as a tool for Integrated Computational Materials Engineering (ICME). The modeling work that has been done has used computationally expensive cohesive zone models (CZM) to simulate microcracking at phase interfaces and within the brittle intermetallic phases [36].

In this paper, ICME tools are established to enable the investigation of the microstructure-sensitive mechanical properties of Mo-Si-B alloys. Four mechanical properties are evaluated: two properties controlled by homogenization, elastic modulus, and yield strength, and two properties controlled by localization, fatigue crack formation, and susceptibility to microcracking, which is inversely related to ductility. For this task, three tools are required: a microstructure generator for creating synthetic volume elements, a constitutive model implemented for a finite element solver, and reduced-order models for evaluation of mechanical properties. A novel reduced-order model is introduced to reduce the computational cost of the evaluation of susceptibility to microcracking at phase interfaces in comparison to cohesive zone models. A parametric study is carried out to demonstrate the use of these tools and to compare the effects of α-Mo Si content and temperature on the four mechanical properties of interest.

Microstructure Generator

The microstructure generator developed for this work is based on an ellipsoidal packing algorithm developed by Przybyla, which includes a simulated anneal algorithm for space filling [37]. This algorithm is related to the work of Groeber et al. [38] in development of the tools packaged in the software package DREAM.3D [39]. The microstructure generator developed for this work is chosen for ease of extending the algorithm to multiple regions with distinct microstructural features in a single volume element, which is important to capture the features of the α-Mo calibration material [40]. The generator also captures the unique traits for separate phases as well as the phase volume fractions for each phase. For each phase, the microstructure generator is capable of capturing crystal structure, mean and standard deviation of grain size, grain shape distribution, grain shape orientation distributions, and orientation distribution.

The crystal structure is captured by passing the phase and its orientation to the constitutive model, which captures the elastic anisotropy and slip systems associated with the crystal structure of that phase. Grain size statistics are defined as a mean and standard deviation for a uniform distribution, which the microstructure generator then converts to a log normal distribution. Grain shape is captured by approximating grains with ellipsoids defined by major and minor aspect ratios which vary according to a beta distribution. The generated ellipsoids are packed in order from largest to smallest for a single phase at a

time. Control over the final features is provided by artificial parameters that reduce the ellipsoidal volumes and phase volume fractions prior to the ellipsoidal packing to account for changes created by the space filling simulated anneal process. Both the ellipsoidal packing and space filling algorithms respect the periodic boundary conditions of the volume elements. Orientation distributions are captured through the free and open source, third party, MATLAB toolbox MTEX [41]. After the space filling algorithm, all of the final microstructural features are verified against the original microstructural description [37, 40].

For this work, the synthetic volume elements are required to be large enough to provide representative volume elements (RVEs) [42] for the mechanical properties of elastic modulus and yield strength demonstrated through convergence studies of mesh refinement and total grain count (volume element size) [40]. Volume elements sufficiently large enough to be considered representative for modeling microstructure-sensitive fatigue crack formation and damage initiation are computationally intractable. Instead RVEs for yield strength are treated as statistical volume elements (SVEs), which capture the locally varying heterogeneous response of the material [43], for fatigue resistance and susceptibility to brittle microcracking.

Three-Phase Mo-Si-B Material

The three-phase Mo-Si-B material synthetic microstructure instantiations are randomly textured, three-phase volume elements with a random spatial distribution of the phases. The characteristics of the synthetic microstructures are chosen to match some of the more promising Mo-Si-B alloys [15, 23, 24]. The parametric study conducted in this work varies two key parameters: volume fraction of each phase and Si content of the α-Mo phase. The variation in Si content is achieved through the calibration of the constitutive model, but the volume fraction of each phase is captured explicitly in the volume element instantiations. For the three-phase Mo-Si-B material in the parametric study, the volume fraction (Vv) of α-Mo is varied from 45 to 80% and the remaining volume fraction is divided between the intermetallics at a constant ratio of 1:2 A15 to T_2 phase to match the approximate ratios found in the reference material [24]. The volume element definitions for the parametric study are presented in Tables 1 and 2. In addition to these parameters, several parameters are held constant for all synthetic microstructures: 33 elements per edge (35,937 total elements) and ellipsoid aspect ratios of 0.80 with a standard deviation of 0.08 for all three phases.

Six separate instantiations are created for each set of parameters in the parametric study. An example instantiation with 63% volume fraction of α-Mo is presented in Fig. 1. The three-phase Mo-Si-B SVEs are 0.09 mm on each edge with 33 elements per edge.

Table 1 Microstructure parameters investigated in parametric study

Parameter	SVE1	SVE2	SVE3	SVE4	SVE5	SVE6
Edge length (mm)	0.090	0.090	0.090	0.090	0.090	0.090
Vv α-Mo	0.45	0.54	0.63	0.71	0.76	0.80
Vv A15	0.37	0.31	0.25	0.19	0.16	0.13
Vv T_2	0.18	0.15	0.12	0.10	0.08	0.07

While each instantiation matches the statistical description of the grain size, grain shape, grain shape orientation, and texture, individual instantiations exhibit locally varying microstructural features that may effect variability in the mechanical properties. Specific features, such as misorientation, have been shown to be important for predicting fatigue response [43] and may be anticipated to effect damage formation as well. The purpose of these multiple instantiations is to investigate the sensitivity of the mechanical properties to the locally varying inhomogeneity of the microstructure.

Constitutive Model

A crystal viscoplastic model is used for all three phases of the three-phase Mo-Si-B alloy, with unique parameter sets for each phase [40]. The model includes the fully anisotropic elasticity tensors, the crystal slip systems, the flow rule, and evolution equations. The relatively hard, brittle, intermetallic phases [3, 30, 32] are treated as purely elastic, while the relatively ductile α-Mo phase is treated with a full crystal viscoplasticity (CVP) flow rule over the 12 $\{100\}\langle 111\rangle$ and 12 $\{112\}\langle 111\rangle$ BCC slip systems. The option to build upon this work by including plasticity in the intermetallic phases is maintained by using the full CVP flow rule for these phases, but assigning the calibration parameters in such a way that plasticity is inactive. The full development and calibration of the α-Mo phase model parameters from polycrystalline experimental data is presented elsewhere [40].

The flow rule used in this work is an extension of the crystal plasticity flow rule developed by Pierce et al. [44]

Table 2 Fixed microstructure parameters in parametric study

Parameter	α-Mo	A15	T_2
Mean dia. (μm)	10	8	8
std. dev. dia. (μm)	2	1	1

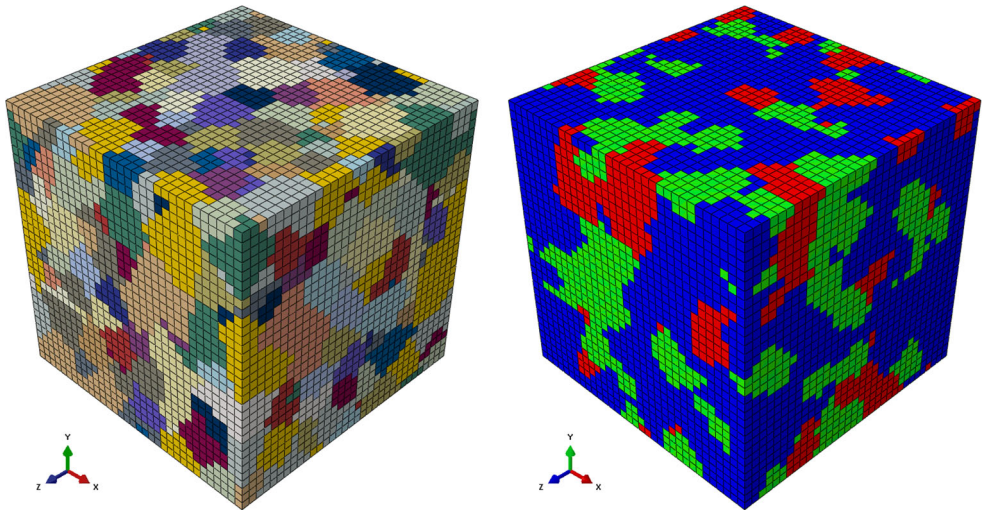

Fig. 1 Three-phase Mo-Si-B synthetic microstructure with 63% volume fraction α-Mo

(a) Colors assigned by unique grains

(b) Colors assigned by phase. Blue: α-Mo. Green: A15. Red: T_2.

and is chosen for its wide use in metal crystal plasticity models [45–47]. The flow rule is defined as

$$\dot{\gamma}^{\alpha} = \dot{\gamma}_0 \left\langle \frac{|\tau^{\alpha} - \chi^{\alpha}| - \kappa^{\alpha}}{D^{\alpha}} \right\rangle^{\frac{1}{m}} \operatorname{sgn}\left(\tau^{\alpha} - \chi^{\alpha}\right) \tag{1}$$

where α is a slip system index, $\dot{\gamma}^{\alpha}$ is the inelastic shear strain rate on the αth slip system, $\dot{\gamma}_0$ is the reference inelastic shearing rate, τ^{α} is the resolved shear stress on the αth slip system, and χ^{α}, κ^{α}, and D^{α} are the current values of back stress, threshold stress, and drag stress on the αth slip system, respectively. The $\langle\rangle$ brackets are Macaulay brackets and sgn () returns positive or negative unity, depending on the sign of the term in parentheses. The variable m in the exponent is the strain rate sensitivity exponent. Both $\dot{\gamma}_0$ and m are material parameters that are typically treated as constants, but can vary with microstructure and temperature. For the α-Mo phase, it is assumed that the 12 $\{100\}\langle 111\rangle$ and 12 $\{112\}\langle 111\rangle$ BCC slip systems are active.

Back stress, threshold stress, and drag stress may all evolve over the course of loading. Depending on the material under consideration, many different types of equations have been used for the evolution of back stress, threshold stress, and drag stress. For back stress and drag stress, the most common evolution equations follow the direct hardening, dynamic recovery form of the Armstrong-Frederick equations [48].

For the α-Mo phase, the drag stress is treated as a non-evolving constant dependent on temperature and Si content and back stress evolves as

$$\dot{\chi^{\alpha}} = B\dot{\gamma^{\alpha}} - C\chi^{\alpha}|\dot{\gamma^{\alpha}}| \tag{2}$$

where B and C are functions of temperature and Si content. The reference inelastic shearing rate $\dot{\gamma}_0$ is also a function of temperature and Si content and the strain rate sensitivity exponent m is a function of Si content. The threshold stress κ^{α} can also be an evolving function of temperature, Si content, and grain size. However, the threshold stress is not used because temperature and solid solution hardening are already captured in the drag stress and studies of the Hall-Petch effect in α-Mo have shown inconsistent results with some studies showing no Hall-Petch behavior at grain sizes as small as 50 µm [25, 49, 50].

The strain rate sensitivity exponent accounts for differences in yield strength as a function of strain rate, and back stress evolution is used to calibrate the plastic hardening behavior. Since no single crystal information is available for the α-Mo phase to individually calibrate each slip system, all 24 slip systems are treated with the same parameter set; however, the model implementation retains the option of treating up to three separate types of slip systems with unique calibrations and can be extended to treat each system individually.

One limitation of this constitutive framework is the inability to investigate the dislocation mechanisms of BCC metals. There are two crystal plasticity frameworks that directly address the dislocation physics of Mo, such as twinning/anti-twinning asymmetry and non-glide stresses [51, 52]; however, these works are limited to relatively low temperatures and to pure Mo. While these frameworks are not adopted for the broad parametric study presented here, future investigations targeting specific microstructures should include these effects by extending those frameworks to higher temperatures and Mo-Si solid solutions.

Because stress-strain information available for the α-Mo phase is limited to monotonic uniaxial compression and tension tests [25, 40], no calibration can be made for the cyclic response. Instead, it is assumed that the material

Table 3 Elasticity tensor component regressions as a function of temperature (°C): $y = Mx + b$

Component			α-Mo	A15	T_2
C11	M	$\left[\frac{\text{GPa}}{^\circ\text{C}}\right]$	−0.0578	−0.0578	−0.0460
	b	[GPa]	463.0	506.3	492.7
C12	M		0.0058	0.0058	0.0037
	b		157.5	79.9	164.0
C13	M		–	–	−0.0017
	b		–	–	196.4
C33	M		–	–	−0.0247
	b		–	–	420.4
C44	M		−0.0102	−0.0102	−0.0212
	b		109.1	130.2	180.1
C66	M		–	–	−0.0198
	b		–	–	148.3

is cyclically stable and the stabilized hysteresis curve is obtained from the monotonic calibration.

The constitutive equation is implemented as a User Material subroutine (UMAT) for the general-purpose finite element code ABAQUS [53]. The specific Fortran code used in this work is based on one for γ-TiAl alloys [54] and has been modified for α-Mo by adding the appropriate slip systems, evolution equations, the evolution equation derivatives, and temperature dependence for the elastic and thermal properties.

Elastic and Thermal Properties

The fully anisotropic elasticity tensors and coefficient of thermal expansion for each phase are obtained from literature data [29, 32, 55]. The elasticity tensor of Mo is known from room temperature to 700 °C [55]. To use the constitutive model at higher temperatures, the elasticity tensor components are fit with a linear regression as a function of temperature and extrapolated to 1400 °C. Although the majority of the parametric study is for Mo with Si in solid solution, it has been shown that the addition of Si up to 1.0 wt% has very little effect on the elastic modulus [25]. Consequently, the assumption that the elastic and thermal properties of α-Mo are unaffected by Si content is reasonable.

The elasticity tensor components for the T_2 phase are also known as a function of temperature up to 1100 °C [32]. The elasticity tensor is similarly fit with a linear regression and extrapolated to 1400 °C for this phase. The elasticity tensor components for the A15 phase are only known at room temperature [29], so some assumption about the temperature dependence must be made. In this work, the slope of the linear regression is obtained from the BCC Mo data for the matching cubic symmetry and used to extrapolate the cubic A15 elasticity tensor components to higher temperatures. Other work has used the temperature dependence of the T_2 phase to extrapolate isotropic elasticity constants for the A15 phase [56]; however, the temperature dependence prescribed for each phase was similar. It is worth noting that the elastic properties of the covalently bonded A15 phase may be less sensitive to increasing temperature than the Mo phase. The equations defining the elasticity tensor components are given in Table 3.

Viscoplastic Properties: α-Mo

The α-Mo phase model parameters are calibrated from a mixture of polycrystalline α-Mo experimental data [25, 40] and presented in Tables 4, 5, and 6. The values presented here are calculated for use in the three-phase

Table 4 Initial drag stress, D_0, for α-Mo

Initial drag stress, D_0 (MPa)						
Temperature (°C)	Si content (wt%)					
	0.00	0.10	0.25	0.50	0.75	1.00
25	156.2	134.3	181.3	259.7	334.6	409.4
1400	17.8	50.7	70.3	102.9	159.3	215.7

Table 5 Back stress direct hardening, B, for α-Mo

Back stress direct hardening, B (MPa) with fixed back stress dynamic recovery, $C = 10.0$ [–]						
Temperature (°C)	Si content (wt%)					
	0.00	0.10	0.25	0.50	0.75	1.00
25	5000.0	5000.0	4788.8	4436.9	4211.7	3986.5
1400	2258.9	2258.9	2258.9	2258.9	2258.9	2258.9

Mo-Si-B microstructure simulations from the development and calibration of the α-Mo constitutive law presented elsewhere [40]. In this work, the Si content is assumed to be uniform throughout the α-Mo matrix as well as within each α-Mo grain. While this is consistent with the calibration to polycrystal α-Mo data [25], future work can use the framework developed here to further explore the effects of Si segregation and distribution.

Linear interpolation is first carried out by temperature, and then by Si content, except for the initial drag stress, D_0, at 1400 °C where it is found that a power law made a better fit than a linear regression as a function of temperature at fixed Si content. For linear interpolation at a Si content below 0.29 wt% (Mo-0.29Si), the calibration is extrapolated from Mo-0.29Si and Mo-0.40Si instead of interpolating between Mo-0.00Si and Mo-0.29Si. This is necessary because the addition of small amounts of Si in solid solution changes the dominant deformation mechanism of Mo.

The transition from solid solution softening to solid solution strengthening with increasing temperature is related to a transition temperature where the double kink mechanism no longer dominates plastic deformation and the mobilities of edge and screw dislocations become similar [25]. Consequently, solid solution softening is only observed near room temperature and lower temperatures. These sub-structure effects are homogenized in the Si content and temperature sensitive calibration of the constitutive model parameters for the α-Mo flow rule and evolution equations [40].

Parametric Study of Three-Phase Mo-Si-B

The parametric study is designed to help determine an optimized three-phase Mo-Si-B microstructure that balances strength, fatigue resistance, and susceptibility to brittle microcracking. The α-Mo phase volume fraction varies from 0.45 to 0.8, with the intermetallic phases maintaining a constant ratio of 2:1 A15 to T_2 phase to fill the remaining volume. The Si content of α-Mo varies from 0.0 to 1.0 wt% Si to cover the full range of Si content possibly present in three-phase Mo-Si-B alloys. Each microstructure has a random texture with randomly orientated grain shapes because most feasible processing methods result in such a microstructure. Six sets of volume elements are created according to the microstructure characteristics shown in Table 1. To examine the effects of the volume element instantiations themselves, six separate synthetic volume element instantiations are created for each microstructure definition.

The parametric study is carried out at room temperature and 1400 °C. A representative microstructure is taken from Jain and Kumar [15] and from sample material provided by Pratt and Whitney to ensure the synthetic microstructures closely match promising Mo-Si-B microstructures. In the Jain and Kumar microstructure, the α-Mo phase has an average grain diameter of 20 µm and a volume fraction of 0.511, while the intermetallic phases have grain diameter averages of 15 µm with 0.170 volume fraction Mo_3Si and the remainder made up of the T_2 phase.

The simulation consists of one fully reversed cycle with strain controlled loading to a mechanical strain amplitude of 0.5% applied along the Y-axis (vertical direction in Fig. 1). Periodic boundary conditions are applied to all six faces of the SVE, consistent with the periodic packing of ellipsoids in the microstructure generator. Rigid body motion is eliminated by fixing a corner node on the negative Y face of the model. Loading is applied through displacement along the global Y-axis of a corner node on the positive Y face.

Table 6 Strain rate sensitivity exponent, m, for α-Mo

Strain rate sensitivity exponent, m [–] with a fixed reference shearing rate, $\dot{\gamma} = 0.001 \left[\frac{1}{s}\right]$						
Temperature (°C)	Si content (wt.%)					
	0.00	0.10	0.25	0.50	0.75	1.00
25	6.0	20.0	20.0	20.0	20.0	20.0
1400	20.0	6.0	6.0	6.0	6.0	6.0

An example macroscopic stress-strain response generated by a simulation for the 63% α-Mo SVE for the different Si contents at room temperature is shown in Fig. 2. This figure shows solid solution softening of the α-Mo phase at room temperature where the yield strength of the Mo-0.10Si α-Mo is lower than that of the Mo-0.00Si α-Mo. This is caused by changing deformation mechanisms with increased temperature and Si content as previously discussed. Although solid solution softening is observed experimentally at room temperature, it is not seen at high temperature [25].

Elastic Modulus

The elastic modulus of the simulation is determined from the volume averaged stress-strain response in the elastic portion of initial loading. The elastic modulus predictions as a function of α-Mo volume fraction at both room temperature and 1400 °C are presented in Fig. 3. Because the elastic tensor properties of α-Mo are assumed to be invariant with α-Mo Si content, the elastic modulus predictions do not vary with α-Mo Si content. Each data point in Fig. 3 represents the mean modulus calculated from six instantiations of the same microstructural parameters. The vertical bars represent two standard deviations of the predicted elastic modulus over six instantiations. The ellipsoidal packing algorithm does not precisely match the target phase volume fractions. The horizontal bars reflect two standard deviations of the final α-Mo volume fraction over six instantiations.

Figure 3 shows that the volume averaged elastic modulus is consistent between SVE instantiations targeting the same

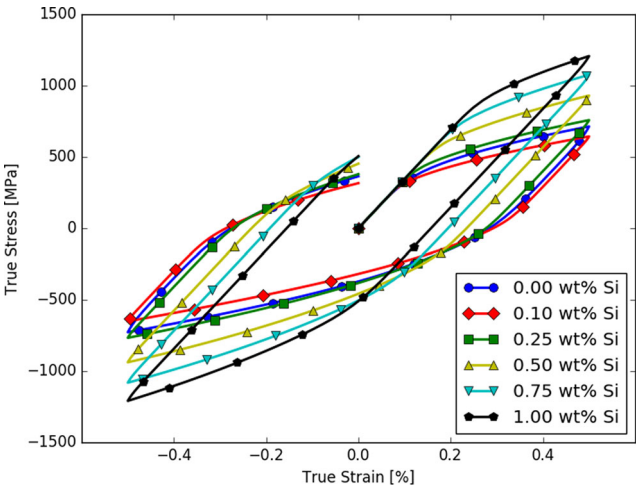

Fig. 2 Cyclic stress-strain response of three-phase Mo-Si-B SVE with 63% volume fraction α-Mo as a function of Si content at room temperature

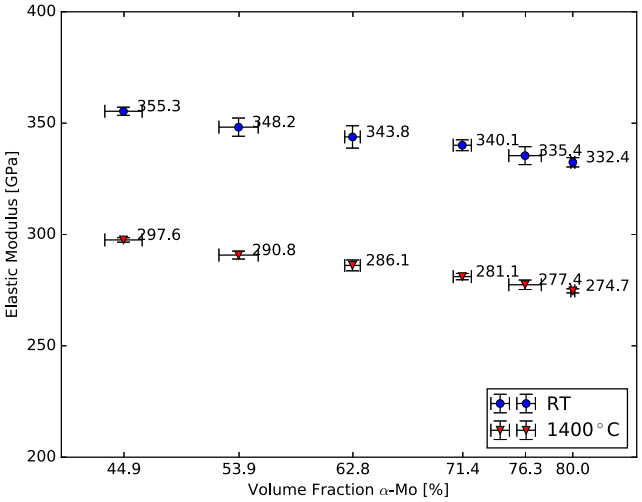

Fig. 3 Predicted mean elastic modulus for six instantiations of each α-Mo volume fraction with a Mo-0.00Si α-Mo CVP parameter set. Bars represent two standard deviations

α-Mo volume fraction, despite the relatively large variation in final volume fraction. Better control over the variation in final α-Mo volume fraction requires a significant increase in SVE volume. However, there is a clear and correct trend of decreasing modulus with increasing α-Mo volume fraction. Therefore, the volume element instantiations are considered to be sufficiently accurate to the target volume fraction for the purposes of this broad microstructure study.

Yield Strength

Yield strength is calculated as a 0.02% offset strength from the volume averaged stress-strain response. Figure 4 presents the uniaxial yield strength predictions as a function of α-Mo volume fraction and temperature for the Mo-0.00Si and Mo-0.50Si α-Mo. As with the elastic modulus predictions, the yield strength shows very little variation as a function of instantiation at each combination of α-Mo volume fraction and α-Mo Si content. The simulations also capture the expected trends of decreasing strength with increasing α-Mo volume fraction and decreasing strength with increasing temperature.

Figure 5 presents the representative yield strength predictions as a function of Si content and temperature at 63% α-Mo volume fraction. Except for the softening at room temperature for small Si content, the yield strength increases with increasing Si content at both temperatures. Comparing Figs. 4 and 5, it is evident that the yield strength of the three-phase material is more dependent on the Si content of the α-Mo phase than on the α-Mo phase volume fraction.

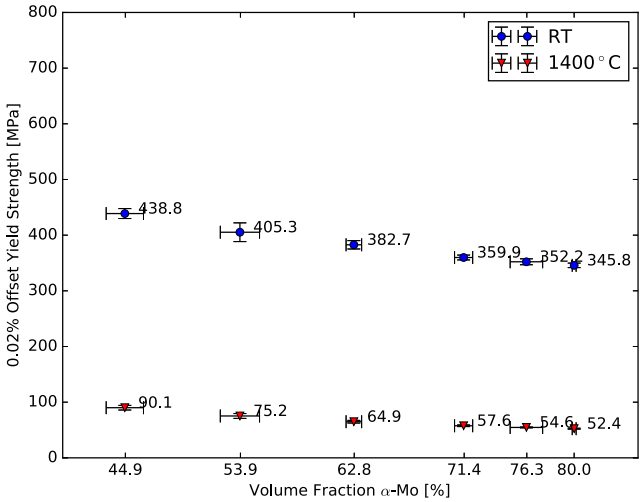

(a) Mo-0.00Si CVP parameter set

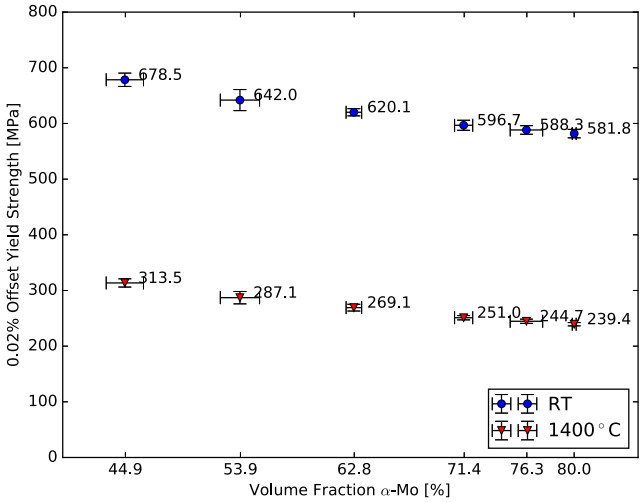

(b) Mo-0.50Si CVP parameter set

Fig. 4 Predicted mean 0.02% offset yield strength for six instantiations of each α-Mo volume fraction. Bars represent two standard deviations

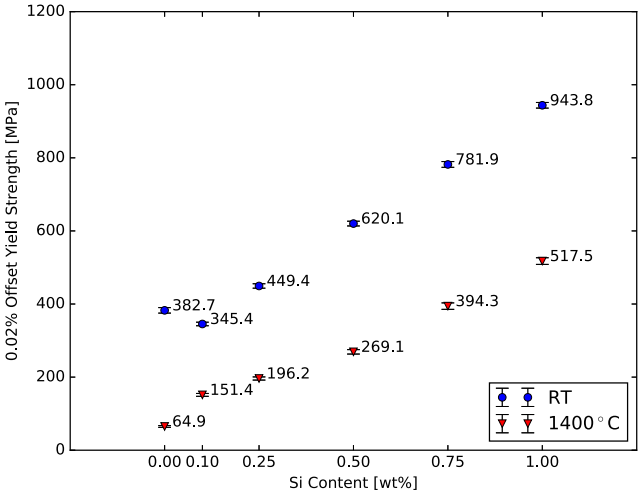

Fig. 5 Predicted mean 0.02% offset yield strength for six instantiations of each α-Mo Si content at 63% volume fraction α-Mo. Bars represent two standard deviations. Note the stronger dependence of yield stress on α-Mo Si content than on α-Mo phase volume fraction

Fatigue Resistance

Fatigue crack formation is controlled by the localized cyclic response in the microstructure. The computational method used to evaluate fatigue resistance compares the driving force against critical driving force required for fatigue crack formation. The driving force is measured through fatigue indicator parameters (FIPs). The possible microstructure dependence of the critical driving force for fatigue crack formation is not addressed in this work. Consequently, the results in this section can only be treated as direct comparisons of fatigue resistance under the assumption that the driving force for fatigue crack formation is strongly dependent on microstructure, while the critical driving force for crack formation is not dependent on microstructure.

Two FIPs are used in this study, the Fatemi-Socie (FS) parameter and the effective cumulative plastic strain (ECPS), which have been shown to correlate well with both low and high cycle fatigue [43, 57–60]. The effective cumulative plastic strain parameter accounts for cyclically accumulated plastic strain and the Fatemi-Socie parameter includes the effects of normal stress at fatigue crack formation sites. The FIPs are calculated from the stress-strain response of a single, fully reversed fatigue cycle with a macroscopic mechanical strain amplitude of 0.5%. The calculation is performed at each integration point prior to performing a local volume average over a grain volume, which is consistent with the volume involved in fatigue crack formation in similar brittle material systems. In this work, the local volume averaging is performed using a Gaussian filter where the length scale is adjusted by setting the standard deviation of the filter to half of the mean α-Mo equivalent grain radius.

Due to the localization problem of fatigue crack formation, a proper treatment of fatigue requires several hundred SVE instantiations for each combination of microstructural parameters, α-Mo CVP parameter set, and loading conditions [43, 47]. Approaching such a study with crystal plasticity is computationally expensive, so recent efforts have pursued reduced-order methods instead [61]. The breadth of microstructures in this study limits the fatigue resistance analysis to a small number of SVEs and a single loading condition. Instead of the usual extreme value approach, this study presents the results of instantiation volume averaged FIPs to capture the general trends microstructure effects for the purposes of efficient, multi-property, microstructure optimization with

the understanding that a more complete fatigue study will be required as the microstructure optimization is refined.

Figure 6 presents the mean and standard deviation of six instantiations for the volume average FIPs as a function of α-Mo volume fraction for Mo-0.00Si and Mo-0.50Si. Note that for FIPs, a larger value represents greater damage per cycle and therefore less fatigue resistance.

Figure 6a shows that both FIPs predict increasing damage per cycle with increasing α-Mo volume fraction at room temperature. This is explained by greater amounts of cyclic plasticity present in the volume due to a larger volume fraction of the plastically deformable α-Mo phase. At 1400 °C, both FIPs initially increase with increasing α-Mo volume fraction, but transition to decreasing with increasing α-Mo volume fraction at higher α-Mo volume fractions. This indicates a re-distribution in the strain fields at higher α-Mo volume fractions where plastic strain accumulation is less severe, resulting in lower FIP calculations across the SVE on average. The predicted α-Mo volume fraction where the trend changes is 74% for ECPS and 54% for FS. The difference in transition point for ECPS and FS is likely related to the effects of normal stress, indicating a transition to lower normal stresses at crack formation sites that decreases the FS parameter before the ECPS parameter.

In Fig. 6a, the unusually large variation of the mean volume average ECPS prediction for 63% α-Mo volume fraction is the result of a single instantiation with a much lower volume average ECPS. This large difference does not show up at room temperature, and if the instantiation is excluded from the mean and standard deviation calculations, the resulting standard deviation more closely resembles that of all the other predictions on this plot.

The change in variation from room temperature to 1400 °C is accompanied by a shift in the location where the largest maximum valued ECPS is predicted within the outstanding instantiation. Most instantiations predict that the maximum valued FIPs remain in the same grain as a function of temperature, but in this case the grain with the maximum valued ECPS is different at room temperature and 1400 °C. This change in location suggests that the microstructural feature driving fatigue damage has changed with changing temperature. In this case, it is speculated that the outstanding instantiation contains a favorable misorientation distribution that tends to more evenly distribute the accumulated plastic strain.

Figure 7 presents the same volume average FIP predictions as a function of α-Mo Si content and

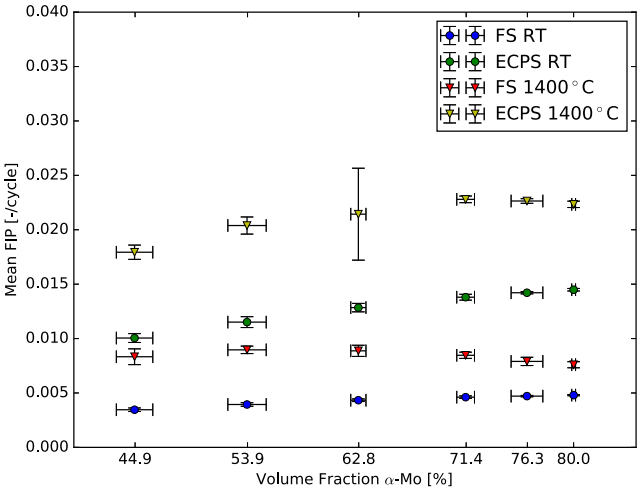

(a) Mo-0.00Si CVP parameter set

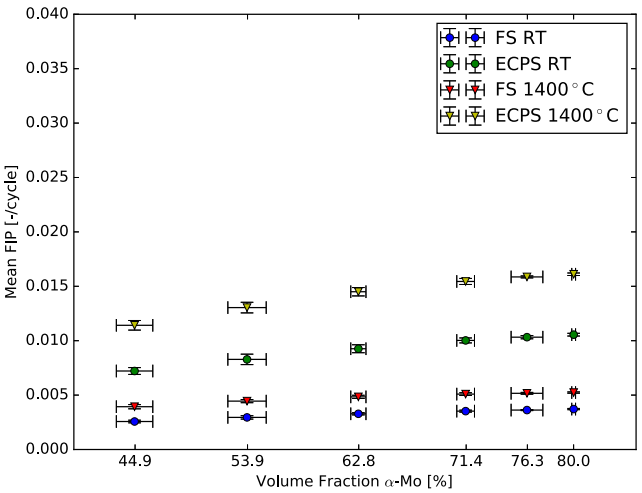

(b) Mo-0.50Si CVP parameter set

Fig. 6 Predicted mean volume averaged FIPs for six instantiations of each α-Mo volume fraction. Bars represent two standard deviations

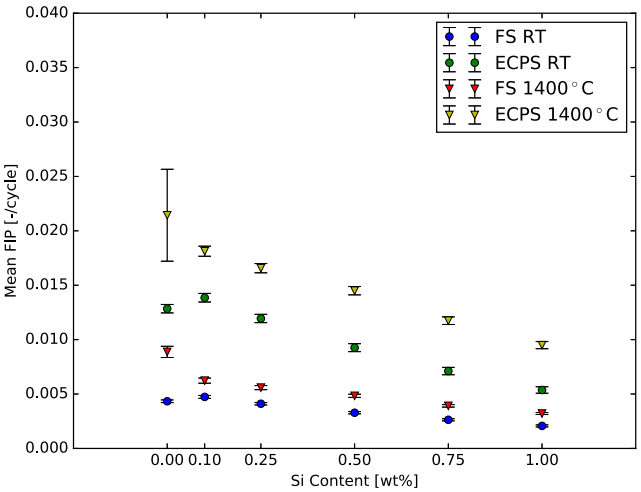

Fig. 7 Predicted mean volume average FIPs for six instantiations of each α-Mo Si content at 63% volume fraction of α-Mo. Bars represent two standard deviations. Note the stronger dependence of FIPs on α-Mo Si content than on α-Mo phase volume fraction

temperature at 63% α-Mo volume fraction. The other α-Mo volume fractions show the same trends as a function of Si content. At room temperature, the solid solution softening demonstrated by α-Mo at 0.1 wt% Si results in increased plasticity and an increase in FIP over pure Mo. Subsequent increases in Si content result in decreasing FIP, where the FIP at 0.25 wt% Si is slightly less than for pure Mo. At 1400 °C, increasing Si content results in decreasing FIP. While less obvious than in the yield strength plots, Figs. 6 and 7 show that the FIPs have a stronger dependence on α-Mo Si content than on α-Mo phase volume fraction.

When comparing the FIP trends as a function of Si content, it is important to remember that these predictions do not necessarily reflect changes in fatigue resistance. Particularly in the case of Mo-0.00Si, it is possible that the critical driving force required for fatigue crack formation is significantly larger than that for α-Mo containing Si. For a more definitive characterization of fatigue resistance, fatigue experiments are required to establish how fatigue resistance changes with α-Mo Si content. However, the results of these simulations provide insight into the microstructure-sensitive fatigue crack driving force, reducing the number of fatigue experiments required.

Susceptibility to Microcracking

Reduced-Order Measure

Modeling tools for predicting the influence of microstructure variation on the susceptibility to brittle microcrack formation in fully 3D simulations are computationally expensive, particularly when modeling weak interfaces with cohesive zone elements in finite element solvers. These tools are less practical for use in microstructure optimization studies with large numbers of simulations spanning large changes in microstructure. It is desirable to develop a reduced-order measure of susceptibility to brittle microcrack formation that can be calibrated from more detailed microstructural models and used in the optimization of mechanical properties as a function of microstructure. Therefore, a new damage indicator parameter (DIP) suitable for use as a quantitative reduced-order indicator of damage formation is developed and validated against cohesive zone element simulations [40].

The method is developed by running two sets of parallel 2D simulations, one with and one without the use of cohesive elements, to evaluate the suitability of a reduced-order DIP for indicating relative susceptibility to brittle microcracking between microstructures. The chosen damage law for the development of a DIP is the same irreversible, bilinear traction-separation damage law used in the cohesive element simulations and shown in Fig. 8

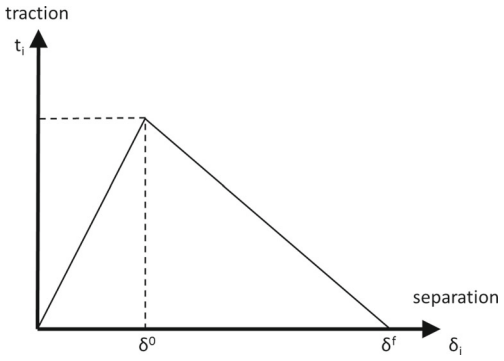

Fig. 8 Bilinear traction-separation CZM

[53, 62]. This cohesive element damage law has been used previously to investigate structure-property relationships in three-phase Mo-Si-B alloys [36], and the development of the DIP follows upon this foundation. The cohesive element model form is

$$t_i = k'\delta_i = (1-d)\,k\delta_i \tag{3}$$

where t_i is the traction on the ith direction, k' is the effective stiffness of a cohesive element, δ_i is the relative displacement or separation between faces of the cohesive element, d is the isotropic damage variable, and k is the original, undamaged stiffness of the cohesive element.

The relevant damage law for this bilinear traction-separation cohesive zone model is

$$d = \begin{cases} 0; & \delta_i^{max} \le \delta_i^0 \\ \dfrac{\delta_i^f\left(\delta_i^{max}-\delta_i^0\right)}{\delta_i^{max}\left(\delta_i^f-\delta_i^0\right)}; & \delta_i^0 < \delta_i^{max} \le \delta_i^f \\ 1; & \delta_i^{max} > \delta_i^f \end{cases} \tag{4}$$

where d is the damage of the cohesive element ranging from zero to one where unity represents a completely failed element, δ_i^{max} is the maximum effective displacement of the loading history and is required to be positive to maintain irreversible damage, δ_i^0 is the initial effective displacement when damage starts, and δ_i^f is the effective displacement for final failure of the cohesive element.

Damage formation is defined by a maximum nominal stress criterion given in three dimensions by

$$\max\left\{\frac{\langle t_n\rangle}{t_n^0}, \frac{|t_s|}{t_s^0}, \frac{|t_t|}{t_t^0}\right\} = 1 \tag{5}$$

where the angled brackets, $\langle\rangle$, are Macaulay brackets, t_n is the normal traction, t_s and t_t are the shear tractions in the 3D case, and the superscript 0 refers to the traction required to initiate damage. With this damage formation criterion, the subscript i in Eq. 4 refers to the direction of

displacement. In the 2D plane strain case, this corresponds to the normal direction and one shear direction. The damage criterion relates the damage formation displacement to the appropriate traction as

$$\delta_i^0 = \frac{t_i^0}{k} \tag{6}$$

where t_i^0 is the nominal stress at the initiation of decohesion in the ith direction and k is the cohesive zone element stiffness. Using a maximum nominal stress criterion, damage is calculated separately for the normal and shear directions. The final damage used in Equation 3, d, is assigned according to the maximum value from the separate normal and shear damage calculations as

$$d = \max\{d_n, d_s\} \tag{7}$$

where d_n and d_s are the damage calculated from the normal and shear stresses, respectively. Calibration of the cohesive zone model can be found in the work of Patra et al. [36].

Without cohesive zone elements, the DIP must be calculated from the local stress-strain field during post-processing. The damage calculation is carried out on the elements on either side of a location where cohesive zone elements would normally be placed using the properties and local strain tensor of that element. The largest calculated damage between two elements making up an interface is then assigned to that interface as

$$d_j = \max\left\{d_{j_1}, d_{j_2}\right\} \tag{8}$$

where d_j is the damage of the jth interface, d_{j_1} is the damage calculated for the first element making up the interface, and d_{j_2} is the damage calculated for the second element making up the interface.

For this study, the locations of interest are the α-Mo/A15 and α-Mo/T_2 grain boundaries and the intermetallic grains, which were found to be the competing crack propagation paths in two- and three-phase Mo-Si-B alloys [11, 36, 63, 64]. However, predicting the location of cracking in the intermetallic grains without introducing an additional constitutive law governing crack location is difficult without cohesive elements. For preliminary development of the DIP, choosing and calibrating an additional constitutive law were not feasible. Instead, intermetallic cracking is neglected in order to simplify the exercise of developing a reduced order quantitative DIP. This approach is justified by the preferred intergranular cracking observed in both two- and three-phase Mo-Si-B alloys [17, 63–65].

For comparing damage between microstructures, the total damage present in the SVE is calculated from the damage of individual interfaces. Since the damage is only calculated at the α-Mo/intermetallic grain boundaries, an interface average damage may be calculated over the interfaces as

$$DIP_{avg} = \frac{\sum_{j=1}^{N_{Mo/Inter}} d_j}{N_{Mo/Inter}} \tag{9}$$

where DIP_{avg} is a measure of the mean damage over all α-Mo/intermetallic interfaces within the SVE, $N_{Mo/Inter}$ is the total number of interfaces of interest, and d_j is the damage at the jth interface of interest. DIP_{avg} represents the mean damage of the interfaces which are allowed to initiate damage within a single SVE instantiation and has a range of zero to one, with one representing a complete failure of additional load bearing capacity. A simulation with a larger DIP_{avg} at a fixed macroscopic strain would be more likely to develop widespread cohesive element failure in a cohesive simulation. Therefore, a larger DIP_{avg} indicates a greater susceptibility to microcrack formation.

A mean value metric is chosen for comparison over localization metrics, such as the extreme values of local damage d_j, for two reasons: (1) to capture the dependence of fracture on widespread cracking, crack percolation, and crack coalescence and (2) to reduce the computational cost of the large number of instantiations required to properly evaluate extreme value statistics. The full development and validation of the DIP_{avg} as a quantitative reduced-order measure of susceptibility to microcracking are developed elsewhere [40].

The validation of the approach is made by calculating the interface average DIP_{avg} for both the cohesive and non-cohesive simulations. Figure 9 compares the results of

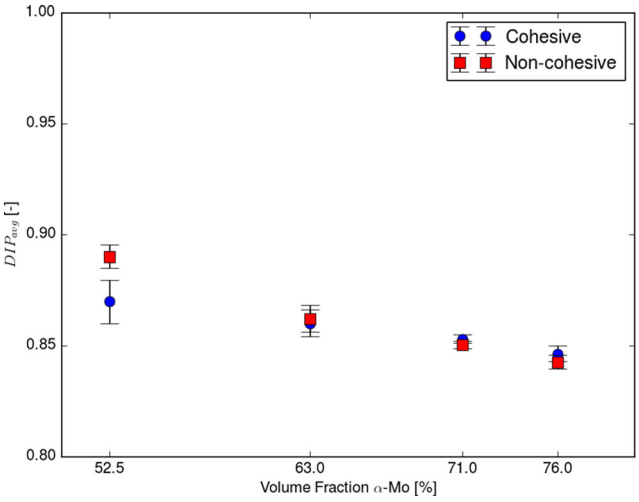

Fig. 9 Predicted mean DIP_{avg} of ten instantiations calculated at 1% macroscopic strain. Bars represent two standard deviations

these simulations as a function of α-Mo volume fraction. Each data point represents the mean of ten instantiations for the same microstructure, and the error bars correspond to two standard deviations. The calculation is performed at 1% macroscopic strain to show the deviation in the DIP_{avg} of the non-cohesive simulations from the DIP_{avg} of the cohesive simulations. This macroscopic strain is approximately 10 times the yield strain and corresponds to the point where widespread cohesive zone element failure has not quite begun for the majority of the simulations.

From Fig. 9, the DIP_{avg} shows the expected trends of decreasing susceptibility to brittle microcracking with increasing α-Mo volume fraction. The DIP_{avg} is inversely correlated with the strain at the maximum tensile stress of the cohesive simulations, which is an indicator of ductility. Thus, the DIP_{avg} correctly indicates increasing ductility with increasing α-Mo volume fraction.

As cohesive elements fail in the cohesive simulations, they leave behind cracks with free surfaces, which are traction free. The stress is redistributed around the cracks in the cohesive simulations but not in the non-cohesive simulations, causing differences in the stress and strain fields. Since the local damage, d_j, is calculated from the traction at the interface elements where cohesive elements are failing, the traction free surfaces in the cohesive simulations reduce the calculated local damage with respect to the non-cohesive simulations. In Fig. 9, the failure of a large number of cohesive elements and the resulting free surfaces are the reason for the difference between the DIP_{avg} of the cohesive and non-cohesive simulations at 52.5% volume fraction α-Mo.

Although the volume average approach with DIP_{avg} is shown to yield good results for ranking relative susceptibility to microcracking, it is anticipated that a more thorough development of the DIP may extend the usefulness of this approach. If the DIP is evaluated according to extreme value statistics and includes the effects of spatial distribution of microcrack formation, it may be possible to capture the percolation threshold of crack coalescence. Such a development would enable use of the DIP to build more detailed structure-property linkages by identifying microstructure characteristics driving microcrack coalescence and the limit of load bearing capacity.

This approach was developed with the intention to reduce computational cost with respect to cohesive zone elements. In the 2D simulations used to develop the DIP, removing the cohesive zone elements reduced computation time by a factor of 2 to 4. Although a direct comparison was not conducted in 3D, it would be expected to see even greater computation time savings. The fully 3D three-phase Mo-Si-B simulations often required 15 h to complete using 16 cpus. With over 200 simulations in the parametric study, this represents a significant reduction in computational cost.

Parametric Study Results

The prediction of susceptibility to microcracking in 3D, three-phase Mo-Si-B simulations was evaluated using the volume averaged DIP_{avg}, calculated at 0.5% macroscopic uniaxial strain. A larger value for DIP_{avg} indicates greater susceptibility to damage formation and is an indicator of a decrease in ductility and damage tolerance. Although the dependence of critical driving force is addressed in the calibration of interface strengths as a function of Si content [36], it is possible that the critical crack driving force depends on additional microstructural features. Therefore, comparing the susceptibility to microcracking with the DIP_{avg} metric requires the assumption that the critical driving force is solely dependent on α-Mo Si content.

Figure 10 presents DIP_{avg} as a function of α-Mo volume fraction at room temperature and 1400 °C for Mo-0.00Si. Figure 10 clearly shows the trends for DIP_{avg} as a function of increasing α-Mo volume fraction at Mo-0.00Si and the same trends are seen at each α-Mo Si content. DIP_{avg} is larger at room temperature than at 1400 °C, which is expected since most materials demonstrate more ductility at high temperatures. At room temperature, DIP_{avg} demonstrates a shallowly decreasing damage with increasing α-Mo volume fraction. At 1400 °C, the same trend is seen, but the decrease in damage is more significant with increasing α-Mo volume fraction. The same general trends hold for Mo-0.10Si through Mo-1.00Si; however, the differences between room temperature and 1400 °C DIP_{avg} decrease with increasing $alpha$-Mo Si content. Additionally, with increasing Si content the decrease in damage with increasing α-Mo volume fraction becomes less significant.

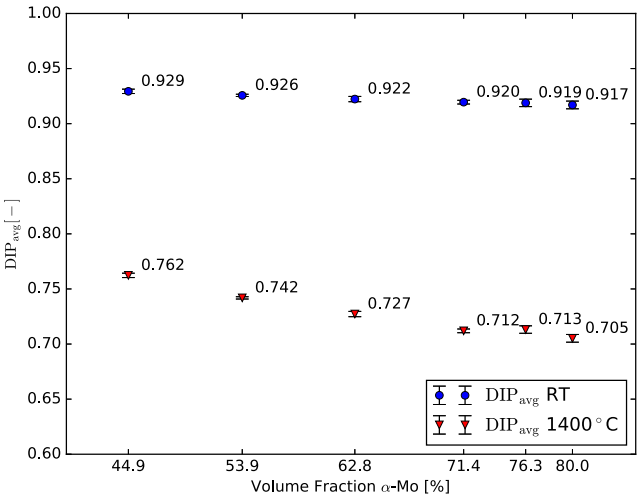

Fig. 10 Predicted mean DIP_{avg} of six instantiations for each α-Mo volume fraction with a Mo-0.00Si CVP parameter set. Bars represent two standard deviations

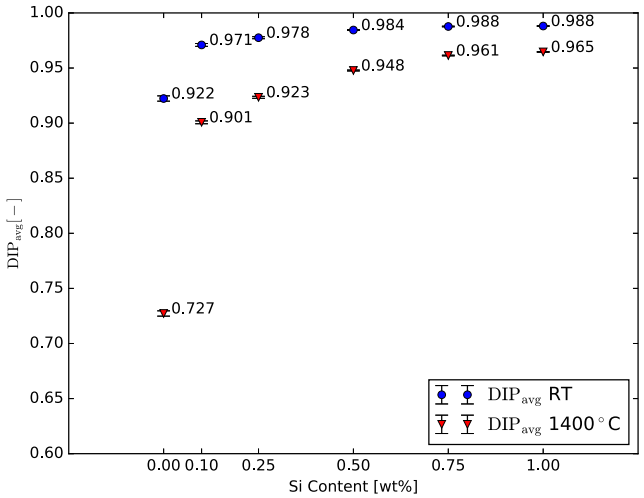

Fig. 11 Predicted mean DIP_{avg} of six instantiations for each α-Mo Si content at 63% volume fraction of α-Mo. Bars represent two standard deviations. Note the stronger dependence of DIP_{avg} on α-Mo Si content than on α-Mo phase volume fraction

Figure 11 clearly shows the trends in DIP_{avg} as a function of Si content at 63% α-Mo volume fraction. These trends are consistent for each α-Mo volume fraction. There is a steep increase in DIP_{avg} from pure Mo with the addition of 0.1 wt% Si, corresponding to a decrease in relative ductility. This large jump in DIP_{avg} is more severe at 1400 °C than at room temperature. From 0.10 to 1.00 wt% Si, DIP_{avg} steadily increases, with smaller increases between the higher Si content α-Mo CVP parameter sets. In fact, at room temperature, DIP_{avg} is nearly invariant between 0.50 and 1.00 wt.% Si in α-Mo. Figures 10 and 11 show that the DIP has a stronger dependence on α-Mo Si content, particularly at low Si content, than on α-Mo volume fraction.

Model Validation

The α-Mo model development includes stress-strain and yield strength comparisons to the limited experimental data available [40]. There is limited availability of stress-strain behavior of fully characterized two- and three-phase Mo-Si-B materials with usable strain measurements in the range used in this study. However, a reasonable comparison of yield strength data can be made against two experimental studies of three-phase Mo-Si-B alloys. Tables 7 and 8 present a comparison of the three-phase Mo-Si-B simulations with the yield strength and available characterization of similar three-phase Mo-Si-B materials from literature [14, 16, 23]. Table 7 also includes modulus comparisons [14, 16].

A relatively recent study on the fabrication, strength, and oxidation of Mo-Si-B alloys includes high-temperature tensile tests of a three-phase Mo-Si-B alloy including the α-Mo, A15, and T_2 phases [23]. However, the tensile tests are performed without a strain measurement and are uncorrected for the test frame compliance, so a direct stress-strain comparison is not useful. An exact match of the experimental microstructures are not included in the parametric study; however, several simulations are close enough to show that the three-phase Mo-Si-B simulations fall in a similar range of strength values. The experimental material has higher yield strengths than both the Mo-0.50Si and Mo-0.75Si α-Mo calibrations for SVEs including 45% and 54% α-Mo volume fraction. This is expected due to the lower experimental test temperature and 0.2% offset yield strength reported; however, a more direct set of simulations would be required to more accurately compare to the experimental material. The reported Si content of the α-Mo phase is not measured directly, so a range of simulations with varying α-Mo Si content would still be required for comparison purposes.

Table 7 Comparison of Middlemas material yield strength to simulated three-phase Mo-Si-B predicted yield strength [23]

Parameter	Simulation				Middlemas [23]		
0.02% offset σ_Y (MPa)	313.5	446.1	287.1	414.9	419*	577*	477*
α-Mo vol. frac. (%)	45.0	45.0	54.0	54.0	47.8	47.8	67.2
A15 vol. frac. (%)	0.37	0.37	0.31	0.31	33.4	33.4	9.2
T_2 vol. frac. (%)	0.18	0.18	0.15	0.15	18.8	18.8	27.3
α-Mo Si content (wt.%)	0.50	0.75	0.50	0.75	0.61**	0.61**	0.61**
Temperature (°C)	1400	1400	1400	1400	1300	1200	1200
Strain rate $\left[\frac{1}{s}\right]$	2.2×10^{-3}	2.2×10^{-3}	2.2×10^{-3}	2.2×10^{-3}	1.0×10^{-4}	1.0×10^{-4}	1.0×10^{-4}

*0.2% offset yield strength reported

**A later study reported the Si content of this material closer to 1.3 wt% Si [18]

Table 8 Comparison of Jéhanno et al. material yield strength to simulated three-phase Mo-Si-B predicted yield strength, continued [14, 16]

Parameter	Simulation				Jéhanno [14, 16]			
Elastic modulus (GPa)	297.6	297.6	290.8	290.8	264	264	259	259
0.02% offset σ_Y (MPa)	90.1	185.9	75.2	165.1	300*	64*	85*	27*
Max σ (MPa)	–	–	–	–	315	102	107	45
α-Mo vol. frac. (%)	45.0	45.0	54.0	54.0	50	50	50	50
A15 vol. frac. (%)	0.37	0.37	0.31	0.31	?	?	?	?
T_2 vol. frac. (%)	0.18	0.18	0.15	0.15	?	?	?	?
α-Mo Si content (wt.%)	0.00	0.10	0.00	0.10	0.01**	0.01**	0.01**	0.01**
Temperature (°C)	1400	1400	1400	1400	1300	1300	1400	1400
Strain rate [$\frac{1}{s}$]	2.2×10^{-3}	2.2×10^{-3}	2.2×10^{-3}	2.2×10^{-3}	1.0×10^{-3}	1.0×10^{-4}	1.0×10^{-3}	1.0×10^{-4}

*Yield strength not reported and stress-strain plot has insufficient strain resolution for accurate 0.02% offset calculation

**As estimated by Patra et al. [36]

A more direct comparison can be made to a study on a similar three-phase Mo-Si-B alloy from the work of Jéhanno et al. [14, 16]. Unfortunately, only the volume fraction of α-Mo is characterized. The relative volume fractions of the A15 and T2 phase and the Si content of the α-Mo phase are not characterized. The probable closest matching material characteristics from this work are presented in Table 8, where an estimation of the α-Mo Si content is taken from Patra et al. [36]. The simulations of this work bounding the α-Mo volume fraction and Si content of the expected values for the Jéhanno et al. material suggest that the Si content estimate is reasonable and that the resulting three-phase Mo-Si-B mechanical behavior is in reasonable agreement given the unknowns in material characterization. The differences in modulus as a function of temperature are likely a result of the unknown volume fractions of intermetallics, but could also result from the unknown texture of the Jéhanno et al. material.

Summary and Conclusions

Research into Mo-Si-B alloys has begun to yield promising results towards using these alloys in gas turbine engines. The work presented here advances the understanding of the microstructure-property relationships of Mo-Si-B alloys by developing and exercising a novel computational approach to microstructure-sensitive mechanical property modeling for Mo-Si-B alloys.

This paper demonstrates that several mechanical properties can be evaluated using a combination of modeling tools, including elastic modulus, yield strength, fatigue resistance, and susceptibility to microcracking. Three tools are used to explore the microstructure-sensitive mechanical properties of three-phase Mo-Si-B alloys: a microstructure generator, a crystal viscoplastic constitutive law, and reduced-order models for evaluating mechanical properties.

A novel damage indicator parameter (DIP) is developed for use as a surrogate for susceptibility to brittle microcrack formation without the use of cohesive elements. This reduced-order modeling approach facilitates the design of fully 3D microstructures using a quantitative measure for relative interface average damage indicator as one of the targeted design objectives in the optimization of multiple mechanical properties.

A parametric study of three-phase Mo-Si-B alloys containing the α-Mo, A15, and T_2 phases is presented to capture the microstructure-sensitive modulus, yield strength, fatigue resistance, and susceptibility to microcracking related to relative ductility. The parametric study explored the effects of α-Mo Si content and phase volume fraction. The yield strength predictions of the parametric study are used to validate the constitutive model of three-phase Mo-Si-B against similar experimental materials.

Since the susceptibility to brittle microcracking, especially at room temperature, is a critically important mechanical property for the high-temperature structural applications of Mo-Si-B alloys, it is found that the Si content of the α-Mo phase is more significant to the alloy's balance of mechanical properties than the α-Mo volume fraction. Consequently, it is recommended that future development work focus primarily on reducing or controlling the Si content of the α-Mo phase. A balance of mechanical properties, then, can be found between 55 and 63% α-Mo volume fraction with as low an α-Mo Si content as possible. In this range of α-Mo volume fraction, oxidation resistance requires further study and must be included in future microstructure optimization work.

These results agree with the findings of experimental work on three-phase Mo-Si-B alloys. The significance of

this work is the development of an efficient computational framework to explore the material design space of Mo-Si-B alloys for multi-property optimization. This framework and the predicted microstructure-property relationships could be refined with additional experiments for calibration and validation of single phase properties, especially for the intermetallic phases. However, the benefit of this ICME framework is the reduction in the number of experiments required to explore the Mo-Si-B material design space.

There are several novel contributions in this work. The crystal viscoplastic constitutive model used in this study is the first crystal plasticity model developed for three-phase Mo-Si-B alloys and the first crystal plasticity model to include Si composition effects and temperatures above 300 °C on the α-Mo phase. A novel reduced-order quantitative damage indicator parameter (DIP) is developed and used to compare susceptibility to microcracking as a function of microstructure. The parametric study is also the first quantitative multi-property microstructure optimization of Mo-Si-B alloys.

Acknowledgments Special thanks to the points of contact during the course of this work, Dr. Gopal Das, Rick Montero, and Dr. Shiela Woodard.

Funding Information This work was supported by United Technologies Corporation, Pratt & Whitney Division.

References

1. Bewlay BP, Jackson MR, Zhao JC, Subramanian PR (2003) A review of very-high-temperature Nb-silicide-based composites. Metall Mater Trans A 34A:2043–2052
2. Dimiduk DM, Perepezko JH (2003) Mo-Si-B alloys: developing a revolutionary turbine-engine material. Mater Res Soc Bull 28:639–645
3. Lemberg JA, Ritchie RO (2012) Mo-Si-B alloys for ultrahigh-temperature structural applications. Adv Mater 24:3445–3480
4. Mitra R (2006) Mechanical behaviour and oxidation resistance of structural silicides. Int Mater Rev 51(1):13–64
5. Aryal S, Gao MC, Ouyang L, Rulis P, Ching WY (2013) Ab initio studies of Mo-based alloys: mechanical, elastic, and vibrational properties. Intermetallics 38:116–125
6. Perepezko JH (2009) The hotter the engine, the better. Science 326:1068–1069
7. Schneibel JH, Kramer MJ, Ünal O, Wright RN (2001) Processing and mechanical properties of a molybdenum silicide with the composition Mo-12Si-8.5B (at. %). Intermetallics 9:25–31
8. Parthasarathy TA, Mendiratta MG, Dimiduk DM (2002) Oxidation mechanisms in Mo-reinforced Mo_5SiB_2 (T2) - Mo_3Si alloys. Acta Mater 50:1857–1868
9. Alur AP, Chollacoop N, Kumar KS (2004) High-temperature compression behavior of Mo-Si-B alloys. Acta Mater 52:5571–5587
10. Alur AP, Sakidja R, Wang P, Jain P, Perepezko JH, Kumar KS (2011) Deformation behavior of a quaternary Mo-Nb-Si-B alloy. In: Materials research society symposium proceedings, vol 1295. Materials Research Society, pp 355–360
11. Choe H, Chen D, Schneibel JH, Ritchie RO (2001) Ambient to high temperature fracture toughness and fatigue-crack propagation behavior in a Mo-12Si-8.5B (at. %) intermetallic. Intermetallics 9:319–329
12. Choe H, Schneibel JH, Ritchie RO (2003) On the fracture and fatigue properties of Mo-Mo_3Si-Mo_5SiB_2 refractory intermetallic alloys at ambient to elevated temperatures (25 °C to 1300 °C). Metall Mater Trans A 34A(2):225
13. Jain P, Alur AP, Kumar KS (2006) High temperature compressive flow behavior of a Mo-Si-B solid solution alloy. Scr Mater 54:13–17
14. Jéhanno P, Heilmaier M, Saage H, Böning M, Kestler H, Freudenberger J, Drawin S (2007) Assessment of the high temperature deformation behavior of molybdenum silicide alloys. Mater Sci Eng A 463:216–223
15. Jain P, Kumar KS (2010) Tensile creep of Mo-Si-B alloys. Acta Mater 58:2124–2142
16. Jéhanno P, Heilmaier M, Saage H, Heyse H, Böning M, Kestler H, Schneibel JH (2006) Superplasticity of a multiphase refractory Mo-Si-B alloy. Scr Mater 55:525–528
17. Kumar KS, Alur AP (2007) Deformation behavior of a two-phase Mo-Si-B alloy. Intermetallics 15:687–693
18. Lemberg JA, Middlemas MR, Weingärtner T, Gludovatz B, Cochran JK, Ritchie RO (2012) On the fracture toughness of fine-grained Mo-3Si-1B (wt.%) alloys at ambient to elevated (1300 °C) temperatures. Intermetallics 20:141–154
19. Liu CT, Schneibel JH, Heatherly L (1999) Processing, microstructure, and properties of multiphase Mo silicide alloys. In: Materials research society symposium proceedings, vol 552. Materials Research Society
20. Nieh TG, Wang JG, Liu CT (2001) Deformation of a multiphase Mo-9.4Si-13.8B alloy at elevated temperatures. Intermetallics 9:73–79
21. Schneibel JH, Kramer MJ, Easton DS (2002) A Mo-Si-B intermetallic alloy with a continuous α-Mo matrix. Scr Mater 46:217–221
22. Kruzic JJ, Schneibel JH, Ritchie RO (2005) Ambient- to elevated-temperature fracture and fatigue properties of Mo-Si-B alloys: role of microstructure. Metall Mater Trans A 36A:2393–2402
23. Middlemas MR (2009) Fabrication, strength and oxidation of molybdenum-silicon-boron alloys from reaction synthesis. PhD Dissertation, Georgia Institute of Technology, Atlanta, Georgia
24. Middlemas MR, Cochran JK (2008) Dense, fine-grain Mo-Si-B alloys from nitride-based reactions. JOM, 19–24
25. Sturm D, Heilmaier M, Schneibel JH, Jéhanno P, Skrotzki B, Saage H (2007) The influence of silicon on the strength and fracture toughness of molybdenum. Mater Sci Eng A 463:107–114
26. Bruckart WL, LaChance MH, Craighead CM, Jaffee RI (1953) Properties of some hydrogen-sintered binary molybdenum alloys. Trans Amer Soc Metals 45:286
27. Northcott L (1956) Molybdenum. Academic Press Inc., New York
28. Saage H, Krüger M, Sturm D, Heilmaier M, Schneibel JH, George E, Heatherly L, Somsen C, Eggeler G, Yang Y (2009) Ductilization of Mo-Si solid solutions manufactured by powder metallurgy. Acta Mater 57:3895–3901

29. Swadener JG, Rosales I, Schneibel JH (2001) Elastic and plastic properties of Mo_3Si measured by nanoindentation. In: Materials research society symposium proceedings, vol 646. Materials Research Society
30. Rosales I, Schneibel JH, Heatherly L, Horton JA, Martinez L, Campillo B (2003) High temperature deformation of A15 Mo_3Si single crystals. Scr Mater 48:185–190
31. Rioult FA, Imhoff SD, Sakidja R, Perepezko JH (2009) Transient oxidation of Mo-Si-B alloys: effect of the microstructure size scale. Acta Mater 57:4600–4613
32. Ito K, Ihara K, Tanaka K, Fujikura M, Yamaguchi M (2001) Physical and mechanical properties of single crystals of the T_2 phase in the Mo-Si-B system. Intermetallics 9:591–602
33. Marshall PE (2015) Development of oxidation resistant molybdenum-silicon-boron composites. PhD Dissertation, Georgia Institute of Technology, Atlanta, Georgia
34. Daloz WL (2015) Developing a high temperature, oxidation resistant molybdenum-silica composite. PhD Dissertation, Georgia Institute of Technology, Atlanta, Georgia
35. Kruzic JJ, Schneibel JH, Ritchie RO (2005) Role of microstructure in promoting fracture and fatigue resistance in Mo-Si-B alloys. In: Materials research society symposium proceedings, vol 842
36. Patra A, Priddy MW, McDowell DL (2015) Modeling the effects of microstructure on the tensile properties and microfracture behavior of Mo-Si-B alloys at elevated temperatures. Intermetallics 64:6–17
37. Przybyla CP (2010) Microstructure-sensitive extreme value probabilities of fatigue in advance engineering alloys. PhD Dissertation, Georgia Institute of Technology, Atlanta, Georgia
38. Groeber M, Ghosh S, Uchic MD, Dimiduk DM (2008) A framework for automated analysis and simulation of 3d polycrystalline microstructures. Part 2: synthetic structure generation. Acta Mater 56:1274–1287
39. Groeber MA, Jackson MA (2014) DREAM.3D: a digital representation environment for the analysis of microstructure in 3d. Integrat Mater Manuf Innov 3:5
40. Brindley KA (2017) Microstructure-sensitive structure-property modeling tools for triplex Mo-Si-B alloys. PhD Dissertation, Georgia Institute of Technology, Atlanta, Georgia
41. Bachmann F, Hielscher R, Schaeben H (2010) Texture analysis with MTEX - free and open source software toolbox. Solid State Phenom 160:63–68
42. Hill R (1963) Elastic properties of reinforced solids: some theoretical principles. J Mech Phys Solids 11(5):357–372
43. McDowell DL, Dunne FPE (2010) Microstructure-sensitive computational modeling of fatigue crack formation. Int J Plast 32:1521–1542
44. Peirce D, Asaro RJ, Needleman A (1983) Material rate dependence and localized deformation in crystalline solids. Acta Metall 31(12):1951–1976
45. No AMC, Ortiz M (1992) Computational modelling of single crystals. Model Simul Mater Sci Eng 1:225–263
46. Zhang M, Zhang J, McDowell DL (2007) Microstructure-based crystal plasticity modeling of cyclic deformation of Ti-6Al-4V. Int J Plast 23(8):1328–1348
47. Priddy MW, Paulson NH, Kalidindi SR, McDowell DL (2017) Strategies for rapid parametric assessment of microstructure-sensitive fatigue for hcp polycrystals. Int J Fatigue, 231–242
48. Armstrong PJ, Frederick CO (1966) A mathematical representation of the multiaxial bauschinger effect, Tech. Rep. GEGB Report, RD/B/N731 Berkeley Nuclear Laboratories
49. Wronski AS, Johnson AA (1962) The deformation and fracture properties of polycrystalline molybdenum. Philos Mag 7(74):213–227
50. Orava RN (1964) Trans Metallur Soc AIME 230:1614
51. Lim H, Battaile CC, Carroll JD, Boyce BL, Weinberger CR (2015) A physically based model of temperature and strain rate dependent yield in BCC metals: implementation into crystal plasticity. J Mech Phys Solids 74:80–96
52. Yalcinkaya T, Brekelmans WAM, Geers MGD (2008) BCC single crystal plascticity modeling and its experimental identification. Model Simul Mater Sci Eng 16:1–16
53. Dassault Systemes: Abaqus v. 6.11-1. 2011. Providence, RI, USA
54. Brindley KA, Neu RW (2015) Progress in structure-property modeling tools for γ-TiAl. In: Symposium on high performance aerospace alloys design using ICME approach, (Orlando, FL, USA), the minerals, metals, and materials society. Wiley, pp 1173–1183
55. Dickinson JM, Armstrong PE (1967) Temperature dependence of the elastic constants of molybdenum. J Appl Phys 38:602–606
56. Biragoni PG, Heilmaier M (2007) FEM-simulation of real and artificial microstructures of Mo-Si-B alloys for elastic properties and comparison with analytical methods. Adv Eng Mater 9(10):882–887
57. Suresh S (1998) Fatigue of materials, 2 edn. Cambridge University Press
58. Manonukul A, Dunne FPE (2004) High- and low-cycle fatigue crack initiation using polycrystal plasticity. R Soc 460:1881–1903
59. Dunne FPE, Wilkinson AJ, Allen R (2007) Experimental and computational studies of low cycle fatigue crack nucleation in a polycrystal. Int J Plast 23:273–295
60. Socie D (1993) Critical plane approaches for multiaxial fatigue damage assessment. In: McDowell DL, Ellis R (eds) Advances in multiaxial fatigue, ASTM STP 1191. American Society for Testing and Materials, pp 7–36
61. Paulson NH, Priddy MW, McDowell DL, Kalidindi SR (2018) Data-driven reduced-order models for rank-ordering the high cycle fatigue performance of polycrystalline microstructures. Mater Des 154:170–183
62. Camanho PP, Dávila CG (2002) Mixed-mode decohesion finite elements for the simulation of delamination in composite materials. Tech. Rep. TM-2002-211737 NASA
63. Alur AP, Kumar KS (2006) Monotonic and cyclic crack growth response of a Mo-Si-B alloy. Acta Materiala 54:385–400
64. Kumar S, Alur AP (2007) Crack growth behavior in a two-phase Mo-Si-B alloy, vol 980 of materials research society symposia proceedings. Materials Research Society Cambridge University Press
65. Yu JL, Li ZK, Zheng X, Zhang JJ, Liu H, Bai R, Wang H (2012) Tensile properties of multiphase Mo-Si-B refractory alloys at elevated temperatures. Mater Sci Eng A 532:392–395